Applied Energy 393 (2025) 125983

Contents lists available at ScienceDirect

Applied Energy

journal homepage: www.elsevier.com/locate/apenergy

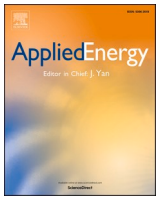

Uncovering the electrochemical processes and understanding the causes of the degradation via EIS-DRT in large-scale solid oxide fuel cell

Patryk Błaszczak [a,b,*], Pyry Mäkinen [c], Aleksander Mroziński [d], Agata Ducka [a], Grzegorz Jasiński [b], Olli Himanen [c], Piotr Jasiński [b]

[a] Advanced Materials Center, Faculty of Applied Physics and Mathematics, Gdansk University of Technology, 80-233 Gdańsk, ul. G. Narutowicza 11/12, Poland
[b] Advanced Materials Center, Faculty of Electronics, Telecommunications and Informatics, Gdansk University of Technology, 80-233 Gdańsk, ul. G. Narutowicza 11/12, Poland
[c] VTT Technical Research Centre of Finland, Espoo, Finland
[d] Faculty of Mechanical Engineering and Ship Technology, Gdansk University of Technology, 80-233 Gdańsk, ul. G. Narutowicza 11/12, Poland

HIGHLIGHTS

- SOFC with a cathode surface area of 100 cm^2 was subjected to a 1700 h test.
- An 'electrochemical fingerprint' of a large-scale cell was described.
- In situ stack characterization was introduced by means of EIS-DRT.
- The degradation issues of the cells in the stack were investigated.

ARTICLE INFO

Keywords:
SOC
Impedance
DRT
EIS
ADIS
Electrochemistry

ABSTRACT

Inducing changes in performance and observation of electrochemical processes is quite easy to do using 'button cells', which are the favorite objects in most research studies. Unfortunately, those cells may sometimes provide misleading outcomes or lead to promising results, applicable only on small scale, belittling their technological value. In this study, a large-scale SOFC with a 100 cm^2 cathode active surface area was subjected to 1700 h working time tests. After the stabilization period, a series of EIS measurements was taken under various changes in operational conditions. Variations in multiple parameters such as pO_2, pH_2, pH_2O, drawn current, or working temperature were introduced to provide an 'electrochemical fingerprint' of the large-scale cell. The impedance data was processed via equivalent circuit fitting and DRT analysis. It was possible to assign the electrochemical and transport processes to the corresponding peaks in the DRT spectra. A clear separation of the peaks originating from diffusion and charge transfer-related resistances was obtained. The single-cell tests allowed for the analysis of the actual state of the repeating units in the working 15-cell stack. The material causes of the changes in the performance of the cells were found to be mostly related to changes in the microstructure of the anode via Ni migration and unwanted diffusion of LSC-born elements such as Co segregation or the formation of the SrO-ZrO_2 phases. Furthermore, the degradation issues of the cells in the stack differ depending on the placement due to the formation of the hotspot in the central part.

1. Introduction

The current worldwide energy crisis and geopolitical situation is causing many research groups to concentrate their studies towards finding alternative energy sources and efficient ways to store it. Solid Oxide Fuel Cells (SOFCs) represent one of the most promising groups of electrochemical devices that could be a solution for future energy provision. Due to relatively high operation temperature and the possibility of reversible operation this technology was given a pronounced interest. The switch between the SOFC and SOEC (Solid Oxide Electrolysis Cell)

* Corresponding author at: Advanced Materials Center, Faculty of Applied Physics and Mathematics, Gdansk University of Technology, 80-233 Gdańsk, ul. G. Narutowicza 11/12, Poland.
E-mail address: patryk.blaszczak@pg.edu.pl (P. Błaszczak).

https://doi.org/10.1016/j.apenergy.2025.125983
Received 17 February 2025; Received in revised form 14 April 2025; Accepted 23 April 2025
Available online 10 May 2025

work regimes could potentially be coupled with the intermittent energy sources to match daily fluctuations [1,2]. In general, state-of-the-art SOFC consists of an ion-conducting electrolyte layer sandwiched between two porous electrodes. Over the years, cells evolved by adding functional layers protecting the electrolyte or gradual porosity introduced into both the fuel and air electrodes [3]. Despite promising results from laboratories and high-scale manufacturers, technology must continue to develop degradation rates lower than the ones reported so far, especially when cells are used for water electrolysis [4]. However, the improvement of performance and lifespan relies not only rely on finding better materials but also on a wide understanding of the electrochemical processes happening with working cells. Observation of the real-life operation of the SOCs would offer guidance and target the most crucial limiting aspects for achieving the desired parameters.

Within all characterization techniques, Electrochemical Impedance Spectroscopy (EIS) coupled with Distribution of Relaxation Times (DRT) are one of the most powerful and, at the same time, non-invasive methods for bringing the insights into the electrochemical phenomena happening inside the cells [5–7]. Prior to the development of the DRT technique, the EIS data were traditionally evaluated using the equivalent circuit models (ECMs) that were used to represent the polarization and series resistance of the cells. The overall resistance of the SOCs is, in fact, a very complex issue. Due to the fitting limitations using predefined models and poor knowledge of the electrochemical processes happening on the anode and cathode, the results could lead to unreliable conclusions. The DRT technique helped to deconvolute cumulative sum of the parallel processes seen as a polarization resistance and generate more unambiguous models [5,8,9]. However, it is worth mentioning that DRT is a comparative method which provides valuable information and attribute peaks only if a meaningful comparison is carried out. That is why, despite the important role in the research, the outcomes of the studies involving DRT and EIS methods are not univocal.

In general, five or six processes are normally distinguished within complex DRT spectra, which change in intensity and shift their summit frequency as the measurement conditions change. Proper analysis of the positions and relative changes of the peaks in the spectra can provide reliable data on the main sources of their degradation and failures. In that sense, the use of the EIS and DRT techniques could provide the 'electrochemical fingerprint' to resolve the origins of the specific resistances for various types of the cells. Despite widespread usage, the conditions of the measurements and small lab scale of the tests limit the value of the findings for more industrial application. To achieve profitable data and models, a proper and standardized testing scheme must be introduced at the scale mimicking real-life systems as close as possible.

In this work an innovative approach for in situ stack characterization was introduced by means of EIS-DRT performed on a single cell of the same construct as in the stack.

The main objective of this study was to provide a detailed analysis of electrochemical processes as seen through EIS and DRT techniques. All assumptions regarding the origin of the DRT peaks in the spectra of a single cell were implied for the measurements made on the selected cells embedded in the stack, all of which were made without disruption in its operation. By developing the 'electrochemical fingerprint' of the large-scale cell, it was possible to determine the actual state of the stack. What is more, the differences in the DRT spectra could be distinguished both between the single cell and stack as well as various cells forming the stack.

The results revealed how complex the nature of the processes that occur inside the stack observed through the DRT peaks can be. In addition, a wide palette of characterization methods was utilized to properly correlate the DRT results with degradation issues caused by structural and chemical changes in the cell after work.

2. Experimental

2.1. Single cell structural composition

Large anode-supported cells were delivered by the Elcogen (www.elcogen.com) and on the fuel side were composed of 380 μm Ni-3YSZ ($Y_{0.06}Zr_{0.94}O_2$) anode base layer and thin 15 μm Ni-8YSZ anode functional layer (AFL) owning decreased porosity. The electrodes were separated by ~3 μm dense 8YSZ electrolyte followed by ~2 μm GDC (Gadolinia-Doped Ceria) barrier layer. The bimodal cathode was composed of double-porosity LSC64 layer composed of 15 μm base layer and 10 μm contact layer. Additionally, the Ni porous layer was screen printed on top of the fuel electrode to decrease the contact resistance between the anode and the interconnector mesh. The diameter of the circular cell was 120 mm and the effective cathode area was 100 cm^2.

2.2. Testing rig and startup procedure

The cell was placed inside the open-flange geometry testing rig. The testbed consisted of two alumina interconnectors of circular geometry with machined gas distribution channels and Pt electrical leads. The cell was placed between those alumina interconnectors with an interlayer of Ni and Pt mesh on the anode and cathode sides, respectively. Those acted as the current collectors from the electrodes. The oxidant and fuel inlets were placed symmetrically in the geometric center of the housing and provided a radial distribution of the reactant gases. The cell was placed inside the furnace and compressed using an alumina rod and brass weights. The testing rig was equipped with the power source (Delta Elektronika, The Netherlands), electronic load (Kikusui, Japan), voltage booster (Delta Elektronika, The Netherlands), voltage meter (Keithley, USA), water evaporator unit and a set of mass flow controllers (Bronkhorst, The Netherlands).

The cell was heated under constant flow of 500 $ml{\cdot}min^{-1}$ safety hydrogen (5:95 *v*/v H_2:N_2) to maintain the reducing condition on the anode side and protect the Ni mesh from oxidizing. The cell temperature was increased to 650 °C with 1 $°C{\cdot}min^{-1}$ ramp rate. Ambient air was pumped on the opposite electrode with a fixed flow rate of 500 $ml{\cdot}min^{-1}$. After reaching the desired temperature, the amount of H_2 in the anode feed stream was increased in increments until 100 vol% H_2 concentration was reached. The selected scheme was given by the cell manufacturer and ensured optimal reduction of the NiO-YSZ electrode. The final flows of the fuel and oxidizer streams for all experiments were set to 1 $Sl{\cdot}min^{-1}$ and 2 $Sl{\cdot}min^{-1}$, respectively. The gas feeding rates were chosen based on the previously established nominal operation conditions given by Elcogen, but most importantly, to minimize resistance due to the diffusion in the gas channels, ensure high exchange rates, maintain pseudo-uniform gas composition in the electrode surroundings, and exclude starvation effects, which are of no importance for EIS studies. No gas cleaning buffers were included, and the gases were supplied directly to the electrodes via a heated gas line. Unfortunately, no humidification of the gas below (~10 vol%) was possible within the testing rig. The hydrogen stream was further referred to in the text as pure hydrogen, although a minor water content was present at the anode, mostly because of internal leakage and formation of the water vapor around the housing. The influence of leakages related to cell and housing was limited thanks to the open flange geometry and high flow rates of both oxidant and fuel. Exemplary EIS spectra were also collected for the second cell of the same batch to confirm the reliability of the data.

Prior to the testing regime, the cell was activated and conditioned under nominal operating conditions for 168 h. The cell was operating in SOFC mode under the aforementioned gas flows generating a current density of 250 $mA{\cdot}cm^{-2}$ (25 A total current). During this time the cell voltage was constantly increasing due to the reorganization of the Ni-YSZ cermet material and the growth of Ni grains, which is a common behavior for SOCs during the reduction and the startup [10]. Current-

voltage characteristics (*iV* curves) were collected from the OCV (0 A) up to the nominal operating point of 25 A, with a current increase rate of 1 A·min^{-1}. The values of current, power densities, and impedances were normalized to the cathode area.

The data was constantly collected using dedicated PLC-based control software in the microsecond range. The control software on the test rig was equipped with an alarm and safety modes in case of improper work of the cell or any of the components.

2.3. Electrochemical impedance of single cell and DRT analysis

The impedance spectra were collected using the Reference 3000™ potentiostat from Gamry Instruments Inc. equipped with the Reference 30k™ Booster. The spectra were collected in galvanostatic mode within the frequency range of 100 kHz to 0.1 Hz with 13 points per decade. If not stated differently, all the impedance measurements were performed with the polarization of the cell equal to 0.015 A·cm^{-2} (DC 1.5 A total) in fuel cell mode with proper stabilization time under load prior to applying the AC amplitude. The measurement at low DC drawn current fitting the range of the AC sinusoidal amplitude ensured the EIS collection always to be performed in the SOFC mode. At the same time, the applied load was small enough so that the measurement mimicked the OCV conditions with marginal changes in gas composition and water formation across the cell [11,12]. Additionally, periodic EIS tests of the working stacks should not force cells to reverse the operating mode, which could introduce measurement-related degradation effects. The AC amplitude was set to 0.6 A based on the preliminary scanning results using various settings to provide a well-defined pseudolinear response of the electrochemical system and a satisfactory signal-to-noise ratio. All spectra were also verified prior to any fitting using a linear Kramers-Kronig transformation and impedance data sets with errors above ±1 % were eliminated from further processing. The cell setup provided twisted leads for both current and voltage probes as well as the shortest path from the cell to the spectrometer to limit the inductive contribution of the testing rig. Even though, all the data above 30 kHz was discarded as it was mostly a parasitic inductive signal coming from the test bench i.e., wiring, meshes, and electronic equipment. A high inductive contribution was quantified by measuring the short-circuited housing at high temperature with all balance-of-plant (BoP) equipment attached to the measuring rig. Despite correcting the EIS spectra by subtracting the inductance signal, noticeable distortions in equivalent circuit fitting were observed. Furthermore, the residuals from Kramers-Kronig test (χ^2) revealed values higher than 10^{-6} indicating poor fit quality [13], unless inductance-influenced high frequency datapoints were discarded. To correct the impedance data, an additional small resistor was measured separately to estimate the leakage current. To further increase the viability of the data, during the EIS tests, the external electronic load/power source was unplugged, and the power was dispersed by the spectrometer itself. The equivalent circuit fitting was performed using Elchemea Analytical software developed by DTU Energy, Denmark, and ZView software (Scribner Associates).

The distribution of relaxation times (DRT) computing was performed using DRTtools software based on Tikhonov regularization [14]. The impedance data with the discarded inductance was processed by the discretization method using Gaussian and a regularization parameter of $1{\cdot}10^{-3}$. The DRT spectra were deconvoluted into corresponding processes using purely Gaussian curves. The Gerischer element-related part of the fit was treated as a widened Gaussian.

The difference in impedance spectra (ADIS) analysis was performed by interchanging single variables in SOFC working conditions while keeping the rest of the parameters constant [15,16]. The parameters selected to be varied were as follows: T, I, pO_2, pH_2 and pH_2O. The partial oxygen pressure was altered by diluting compressed ambient air with pure N_2 using flow controllers. Similarly, pH_2 was changed using N_2 mixed with hydrogen before entering the fuel electrode. Water vapor was introduced into the fuel-feeding stream, thanks to the water evaporator followed by the heated transfer line. The temperature of the evaporator was previously optimized to limit the pressure fluctuations that affect the voltage readings. Before all measurements under altered conditions, the cell was allowed to relax until the voltage and temperature readings were fully stable (~1 h). Along with the changes in the chemical potential via gas alterations, a series of measurements under various temperatures were performed in the range of 550–650 °C. For the pO_2 and pH_2 tests, the temperature was kept constant at 650 °C throughout all EIS measurements. Due to the extremely low impedance of the cell in the presence of water vapor, during those tests, the temperature was lowered to 600 °C to improve the EIS responsivity and limit the noise from the spectrometer. The temperature was a reading of the center thermoelement placed at the fuel gas inlet. The set of the varying parameters that were tested to obtain a reliable process map based on the differences in the DRT spectra is summarized in Table 1. Information about directly affected electrode was included.

To further analyze and uncover the chemical processes behind the DRT peaks a series of tests were performed using cells of slightly modified construct compared to large-scale cell. To observe the influence of the anode thickness on gas diffusion, the second cell with a thicker anode (400 μm) was tested using the same procedure. To determine the diffusion related impedances, a series of two button cells (Elcogen Oy) of the same construct as the large-scale, but with two different thicknesses of the LSC cathode, were tested. The tests were carried out on 400 μm anode-supported button cells due to the technical limitations in the manufacturing of the large-scale cells with modified cathode thickness. The button cells were tested on a SOC testing rig (Fiaxel, Switzerland) under the same conditions, but scaled down because of the smaller cell dimensions.

2.4. Stack characterization and EIS spectra collection

The test stack was provided by Elcogen and consisted of 15 cells of the same construct as the one used for single cell studies. Each cell had an active area of 121 cm^2 with all cells connected in series. The stack was tested in a test rig consisting of an external high temperature furnace, stainless steel gas lines providing reactant gases through the mass flow controllers (Bronkhorst, The Netherlands), pneumatic stack pressurizer, electronic load (Kikusui, Japan) and electronic voltage booster (Delta Electronika, The Netherlands). During operation, the stack was fed with air on the cathode and 50:50 *v*/v N_2:H_2 mixture on the anode. All gases were heated before being fed to the stack. During operation, the cells' voltage, gas flows, gas inlet and outlet pressure and temperatures, as well as furnace temperature stack internal temperature, and electric current were constantly monitored.

The test was initiated with a heat up of the furnace to 650 °C (2 °C·min^{-1}) feeding air on the cathode side (33 Sl·min^{-1}) and diluted hydrogen on the anode side (N_2 10 Sl·min^{-1} + H_2 0.5 Sl·min^{-1}). After heating, the nominal flow on the anode side was changed to 15.5 Sl·min^{-1}. After stabilization, performance tests (OCV; *iV* curve; air and fuel utilization) were performed to validate the performance of the stack. After this point, a long-term operation test under 0.25 A·cm^{-1} electric current was performed. During the long-term operation of the stack the temperature of the surrounding furnace was set to 650 °C, which resulted in a real reading from the middle of the stack equal to

Table 1
Selection of the varying parameters during the EIS measurements.

Variable	Values	Unit	Targeted electrode
T	550, 600, 650	°C	Anode/Cathode
I	1.5, 3.0, 5.0, 7.5, 10, 15	A	Anode/Cathode
pO_2	0.05, 0.11, 0.16, 0.21	atm	Cathode
pH_2	0.25, 0.5, 0.75, 1.0	atm	Anode
pH_2O	0.125, 0.25, 0.375, 0.5, 0.75	atm	Anode
TpH_2O	560, 580, 600, 620	°C	Anode/Cathode

~675 °C. The gas inlet temperatures were between 615 and 620 °C.

During the long-term test, EIS measurements were performed with Gamry Reference 3000™ potentiostat for cells No. 5 and No. 8 counting from the bottom of the stack, giving out the data about the middle of the stack and the bottom outer cell. EIS spectra were measured in the frequency range of 0.1 Hz to 100 kHz with 10 points per decade. The EIS measurement setup was constructed, so that the DC current was run through an external electronic load and EIS current leads were connected to the stack terminals in parallel. A small (15 mΩ) resistor was mounted between the stack and the electronic load, allowing to measure a part of the EIS excitation signal that leaks through the electronic load and to correct the datasets. For all measured frequencies, the leakage signal was rather small (below 5 % of the excitation signal) and mostly had any significance only for the measurements points over 10 kHz. Unfortunately, the stack could not be disassembled and characterized after the test.

2.5. Material characterization methods

The diffraction patterns were collected using Bruker D2 PHASER XE-T with a Cu-Kα radiation source both on the anode and the cathode side without prior grinding of the samples. The morphology of the fractured and polished cross-sections of the cells, before and after the reduction as well as post mortem images were taken using Scanning Electron Microscope (SEM, FEI Quanta FEG 250) with the Energy Dispersive X-ray Spectroscope (EDX, EDAX Genesis APEX 2i) and Apollo X SDD detector or Phenom XL (Thermo Fisher Scientific, The Netherlands) instrument with integrated spectroscopy analyzer (Thermo Fisher Scientific, 25 mm^2 Silicon Drift Detector). The cross sections for the imaging were prepared by embedding the cells in epoxy (EpoFix™, Struers) and polishing them down to 1 μm finish.

The specific surface area (SSA) was measured based on the BET isotherm model on the N_2 sorption unit (NovaTouch LX1, Quantachrome). Prior to the sorption measurements, the samples were finely ground and subjected to adsorbate removal under high vacuum at 300 °C for 3 h. Where mentioned, the SSA values were calculated for the BET region of the isotherm and the total pore volume was taken from the pressure point $p/p_0 \approx 1$. The X-ray Photoelectron Spectroscopy (XPS) spectra were collected using Omnicron NanoTechnology X-ray photoelectron spectrometer with a 128-channel collector. XPS measurements were taken under ultra-high vacuum conditions ($<1.1{\cdot}10^{-8}$ mbar). The photoelectrons were excited by an Mg-Kα X-ray source with the anode operating at 15 keV and 300 W. The obtained spectra were analyzed and deconvoluted using the XPSPEAK41 freeware software. Prior to the measurement, the samples of freshly reduced and spent cells were manually ground to fine powder and mounted onto the test plate using carbon tape. The tape was used to calibrate the charging of the sample based on the C1s edge location.

3. Results

3.1. Cell performance during the testing time

The cell was reduced according to the producer's recommendations and reached the desired range of OCV. A preliminary collection of the *iV* characteristics was performed to further check the state of the cell and to prove the proper work of the housing and the cell itself. All delivered parameters were within the normal range ascribed to Elcogen cells. The data regarding recorded values of the voltage, the current and the temperature are shown in Fig. S1. in Supplementary Materials. The cell was subjected to a heavy testing regime involving intermittent work under the nominal SOFC operation conditions: 650 °C furnace temperature, 250 mA·cm^{-2}, 1 Sl·min^{-1} H_2, and 2 Sl·min^{-1} air. The breaks in continuous operation were caused by the EIS measurements at lowered drawn current, as well as testing of the water evaporator setup and external bidirectional power source, which took over the role of main electronic load partially during the tests (EA Elektro-Automatik, Germany). The cell also underwent an emergency shutdown procedure due to a short-term power loss for ~200 h. During all distortions in the operation, the cell was maintained under the flow of 5 vol% H_2/Ar and air but at lowered flow rates due to the existence of automatic emergency protocols. Thanks to that the cell was never reoxidized, and the performance was maintained despite the breaks in the operation, which are inevitable during such a long-term test. All the ruptures in the work of the cell that are clearly visible were indicated and described in Fig. S1. Despite the issues mentioned above, the cell was found to be sturdy and extremely stable during the entire testing time of ~1700 h (period under high temperature conditions). Occasionally, to characterize the performance of the cell, *iV* curves were taken. The *iV* characteristics from 3 different time periods are presented in Fig. 1, after the reduction and stabilization (7 days, 168 h), after 232 h of working (400 h from start), and at the test terminal point (after 1700 h of working time). All *iV* curves were collected up to nominal current with the proper time taken for stabilization. As can be seen in Fig. 1, the performance of the cell increased by a couple percent during the testing time regarding the voltage values under nominal operating conditions of 25 A. The increase was quite prominent during the initial hours, which is a very common behavior for this type of cell, and it is called an activation time. During that time, the anode undergoes changes in microstructure through reorganization of the Ni network and changes in porosity levels [17,18]. This leads to an improvement in the performance of the cells, even for a couple of hundred hours from the starting point of the test. The changes in the microstructure of the Ni-YSZ cermet correlate well with the results of SEM imaging and BET specific surface area postmortem measurements on the spent cell, where it was proven that the size of the pores and Ni grains increased during whole testing time. The findings are

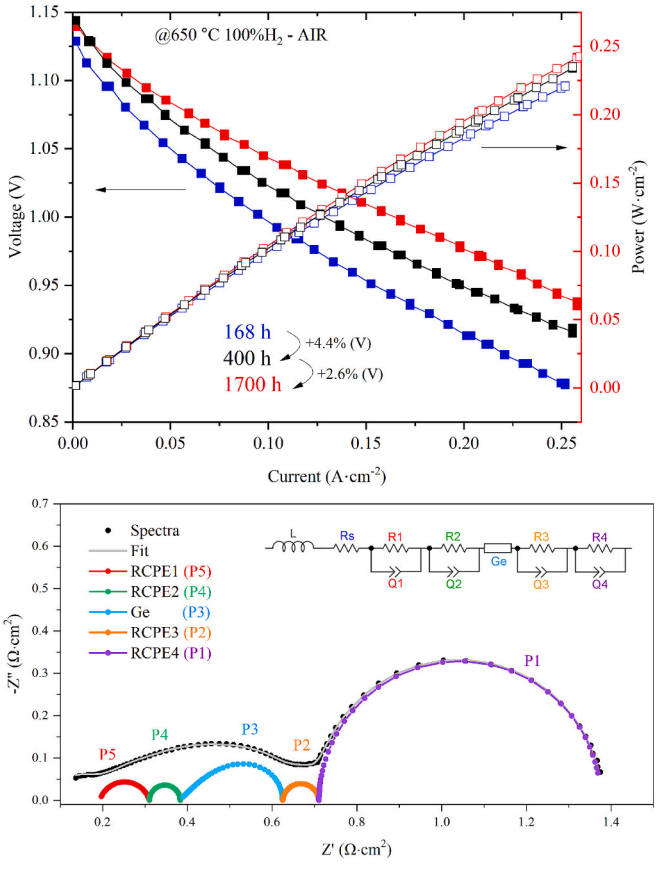

Fig. 1. *iV* and *iP* curves for single cell during the test duration (up) and Nyquist plot of the cell measured at exemplary EIS measurement point with equivalent circuit fitted (down).

described in more detail in Section 3.5. This clearly states that the cell most likely did not undergo visible degradation effects during the testing time, despite harsh conditions and a shutdown procedure. That state-of-the-art single cell came up as a status sample for performing the electrochemical processes deconvolution. In that sense, single cells could be used as a source of 'electrochemical fingerprint' for application in the characterization of working stacks based on the same composition and construction of cells. This approach eliminates the need to perform all the analyzes on the stacks under varying conditions, which might be challenging and laborious.

Nearly invisible deterioration levels were maintained as a result of the usage of proper starting materials, a thin electrolyte, a good quality barrier layer, and a well-prepared cathode. This also implies a decrease in the working temperature to 650 °C, which again limits the unwanted aging of the cell. Furthermore, the cell was kept without the influence of, for example, evaporating Cr species from the interconnects or migration of Si from a sealant material [19]. Those limitations picture clearly show how important a complex view is on the degradation issues, that occur not only at the cell level but also due to the interactions within the components of the stack [20]. Changes in EIS and DRT spectra of the single cell at the starting point and after the testing time will be described further in the text.

3.2. Impedance analysis of the single cell

All retrieved EIS data was validated using the Lin-KK test tool provided by the Karlsruhe Institute of Technology. The exemplary result of the linear Kramers-Kronig fitting can be seen in Fig. S2. The high frequency response of the single-cell EIS measurement was affected each time by the testing rig setup, cabling, and all the imperfections of the electronic equipment. This noise can be observed in Fig. S2. since the Kramers-Kronig residuals start fluctuating at higher frequencies. Furthermore, an additional process P6 (RCPE5) was found each time at high frequency ~ 40 kHz. Based on the work of Wang Y. [5] this process was ascribed to the transport of the ionic species in the cathode. Due to high uncertainty of the high-frequency signal of the EIS the process P6 was eliminated from CNLS fitting and DRT analyzes to prevent drawing false conclusions from ADIS. This process was able to be deconvoluted with high precision in button cells, due to much higher overall impedance. The DRT spectra containing the P6 process are presented in Fig. S3. Eliminating the P6 process from further investigation did not lower the scientific value of the analysis, as other processes are more complex to describe and can carry similar information. In a fully developed diagnostic tool, the process could be implemented within the CNLS fitting depending on the quality of the measured EIS spectra.

According to the tests' outputs, it was decided to set the cutoff frequency at 30 kHz, disregarding the rest of the data points. The usage of a dedicated booster for the impedance spectrometer increased the reliability of the data, by decreasing high-frequency inductive errors. All the datasets considered were treated in the same way. The exemplary EIS spectra of the single cell at 0.015 mA·cm^{-2} in the form of the Nyquist plot are presented in Fig. 1. The DRT analysis involving the ADIS methodology was used to establish the characteristic frequencies of different electrochemical processes prior to the equivalent circuit fitting using the complex non-linear least squares (CNLS) method. An equivalent circuit composed of seven elements connected in series was proposed based on the DRT analysis and the CNLS fitting results. The following symbols on the circuit correspond to: *L* – inductance, *R* – resistance, *Q* – constant phase element (CPE), and *G* – Gerischer element. The *L* element represents the inductance of the testing rig and all the components installed within. The value of R_s was taken from the fit as a theoretical x axis intercept of the high-frequency arc [21]. The resistance of the 8YSZ electrolyte is represented as R_s element. This parameter accounted for most of the ohmic resistance of the cell and might be further improved via the application of thinner electrolyte layers or the utilization of other materials for the construction of the cells. Although so far, 8YSZ is the most common one due to acceptable ionic conductivity, high availability, and good chemical stability that provides mechanical strength under both oxidizing and reducing conditions [22–24]. At high frequency range two processes were distinguished with the summit frequencies around 4 kHz and 1 kHz, corresponding to the O^{2-} ionic conduction through the anode with the main contribution from the Ni-YSZ cermet material and charge transfer reactions occurring at triple phase boundary (TPB), respectively. The middle frequency (~300 Hz) was introduced as the Gerischer element, which was attributed to the overlapping diffusion in the AFL and the cathode linked to oxygen surface reactions. Finally, two additional elements were introduced due to gas diffusion (mass transfer) and gas conversion at the summit frequencies 25–40 Hz and 0.5–1.5 Hz, respectively. The composition of the equivalent circuit was established based on both CNLS fitting and the DRT-ADIS methodology, described in detail below.

Where given, the polarization resistance (R_{pol}) was calculated as a difference of the full real-part impedance (R_{all}) taken as a theoretical x axis intercept of the last low frequency arc and R_s value.

Thanks to the widely detailed DRT analysis of the single cell performed under numerous varying conditions, an interpretation of the EIS spectra accurately describes the complex nature of the undergoing processes within the fuel cell. The equivalent circuit presented in this study is also in line with other findings previously described in the literature concerning the button cell and short stack measurements done e.g. by Drasbæk D. et al. [25].

3.3. Differences in DRT spectra under varying temperature and cell current

Prior to all the atmosphere manipulations, the single cell underwent a characterization under varying temperature in the range of 550–650 °C followed by the tests under different setpoints of drawn current up to 15 A (150 mA·cm^{-2}). The results are presented in Fig. 2. as the DRT spectra with general trends marked with black arrows. To better visualize the changes happening in the DRT spectra they were deconvoluted using Gaussian function fitting. The exemplary fit is presented in Fig. S4. The data on the spider graphs are presented as a relative change of the peak summon frequency position ($P_{i,\ freq}$) or integrated area of the fitted peak ($P_{i,\ res}$) taking as a reference the starting value of the parameter. Each time, the reference value is given in the form of a dashed line equal to 1. This methodology applies to all graphs to come. The errors in the P3 and P4 fits come from a strong overlap of the processes in the spectra. The numerical values of the resistances obtained using the CNLS fitting are given in Table 2. and Table 3.

The change in the temperature of the cell caused a drastic change in the DRT spectra. The most affected peaks were in the middle- and high-frequency regions, which reveals the thermally driven character of those physicochemical processes.

Starting from the fastest process, P5 revealed a gradual decrease in peak intensity when temperature increased with no change in frequency. After cell polarization, P5 remained nearly unchanged. As the amount of hydrogen fed to the cell was in excess, the impedance did not react after the current was drawn. All these observations could be considered as proof that P5 can be ascribed to the ionic conductivity of YSZ (oxygen transport) in the anode strongly affected by the temperature and insensitive to the amount of current drawn. This finding is in line with the number of studies preceding this one [5,11,26].

The lowering of the impedance with simultaneous shift towards higher frequencies is mainly pointing out the increase in diffusion rates as the diffusion coefficients (D_{coeff}) tend to increase when the temperature increases [27]. The fitting revealed the coexistence of two highly overlapping peaks P3 and P4. Based on the behavior of merged middle frequency peak, it was stated that it comes from the superposition of the diffusive part (mainly P3) resulting from the mass transport across the AFL [28] and the cathode (see 3.3.) and charge transfer reactions at the anode (P4). A similar trend as P3 was clearly observed for the P2

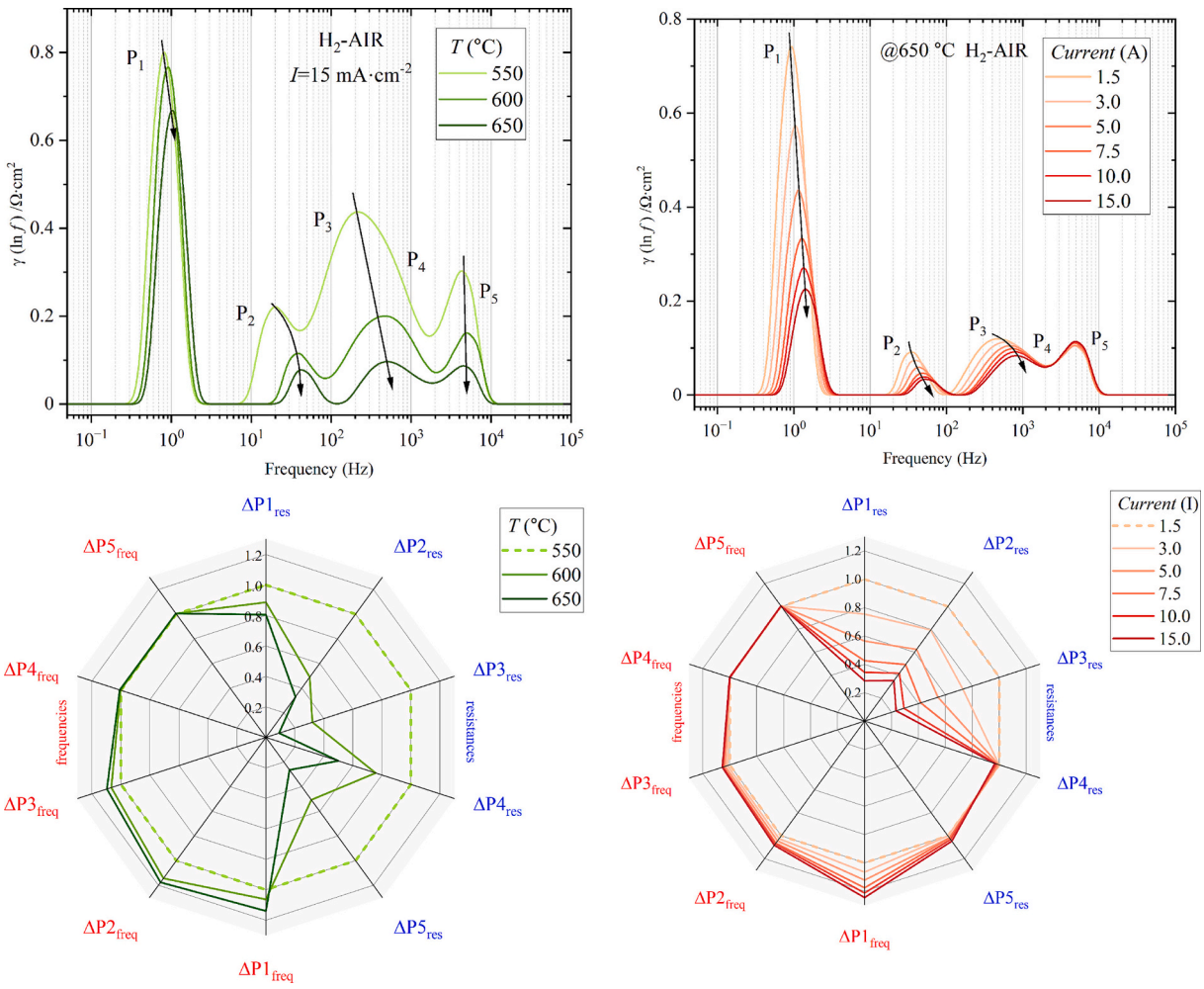

Fig. 2. DRT spectra of the single cell under various temperatures (left) and drawing currents (right) with the corresponding peak changes depicted in spider graph.

Table 2
Results of the CNLS fitting on two extreme conditions of cell temperature with relative change of each resistance (rounded up to full %).

Parameter/ Unit	Value	R_s (mΩ)	R_{pol} (mΩ)	P1 (mΩ)	P2 (mΩ)	P3 (mΩ)	P4 (mΩ)	P5 (mΩ)
T (°C)	550	2.67	28.13	7.37	3.88	4.95	9.66	2.27
T (°C)	650	0.49	12.70	6.01	0.71	0.47	4.77	0.74
ΔR_i (%)		−82	−55	−18	−82	−91	−49	−67

Table 3
Results of the CNLS fitting on two extreme conditions of drown current with relative change of each resistance (rounded up to full %).

Parameter/Unit	Value	R_s (mΩ)	R_{pol} (mΩ)	P1 (mΩ)	P2 (mΩ)	P3 (mΩ)	P4 (mΩ)	P5 (mΩ)
I (A)	1.5	0.71	13.21	6.97	0.79	3.31	0.98	1.16
I (A)	15	0.71	6.39	1.68	0.30	2.15	1.01	1.25
ΔR_i (%)		0	−52	−76	−62	−35	3	8

process, which was ascribed to diffusion in the anode support layer similar to the study by Leonide A. et al. [11] and Caliandro P. et al. [16]. Both diffusive processes reacted strongly to cell polarization, as the concentration gradient of water vapor forming at the reactive sites induced faster exchange of products and reactants, decreasing impedance and forcing the shift to higher frequencies [29].

The highest drop in the peak area was observed for processes P3/P4 and P5, for which the redox reactions and ionic conductivity are highly dependent on thermal activation. The placement of the DRT peaks within specific frequency ranges is also in line with the characterization of the simplified button cells with Pt electrodes studied by Osinkin D.A. [30], where the cathodic and anodic overpotentials were deconvoluted using PrO_x impregnation of the active electrode.

The process introduced as P1 is not as strongly affected as the rest of the processes, as gas conversion is much less directly dependent on temperature and relies on changes in the Nernst potential across the cell. A higher drop in the impedance value is observed when current is applied. It is a direct result of the change in the Nernst potential caused by the production of water vapor at the anode. This behavior strictly follows the results of the numerical model calculations presented in Fig. S5. and the research of Wang Y. et al. [31] during the comparison of the performance tests between button and industrial cells.

3.4. Differences in DRT spectra under varying oxygen or hydrogen partial pressure

To further describe whether the processes have a stronger cathodic and anodic contribution to the overall impedance, tests under varying pO_2 and pH_2 were performed. The results are presented in Fig. 3. Along with the corresponding spider graphs representing relative parameter change and fitted resistance values (see Table 4.)

Referring to the previous statement on the source of the P1 process being gas conversion, it is clearly visible that it is a superposition coming from both the anode and cathode. However, the influence of the oxygen partial pressure of oxygen on the shift and decrease of the peak is quite

weak, compared to the much stronger answer when H_2 is diluted with nitrogen at the fuel electrode. That is, the gas conversion resistance is mostly ascribed to the anode side of SOFC.

Both the diffusion processes P2 and P3 were strongly affected by the change in pO_2 and pH_2. In case of P2, a more pronounced response was observed in case of fuel dilution with a corresponding shift in the peak summon frequency as well as an increase in impedance while depleting the fuel mixture in H_2. It is in line with the behavior of the gas conversion peak, as those two are codependent, as previously described in detail by Jensen M. B. et al. [32]. On the other hand, the P3 peak was nearly insensitive to pH_2 change, but reacted stronger to the change in oxygen content on the cathode side. Thanks to those observations, it was possible to conclude that the P2 process located at lower frequency mainly corresponds to the bulk diffusion process in the anode, while the peak P3 in addition to the diffusion in AFL also includes an additional contribution to the impedance coming from cathodic diffusion processes and/or oxygen adsorption processes. The high responsiveness of the P2 and P3 is also in line with the quantified theoretical changes of the Nernst resistance values presented in Fig. S5., which are connected to the gradients of the partial pressure of water across the fuel electrode.

For the P3/P4 merged processes, the overall impedance value changed slightly compared to the depression of the peak area of the P1 process. Due to that huge difference, the change of the P3/P4 resistance is nearly invisible in the corresponding spider graph.

In contrast, the P4 and P5 peaks were less prone to change when altering pO_2 or pH_2. The feeding gas composition did not cause the starvation effect during the EIS measurements, as the applied DC polarization was far lower than the limiting current. Due to the selected measurement conditions, the charge transfer resistance (P4) and O^{2-} transfer (P5) were left nearly unchanged during those tests. Further deprivation of oxygen and hydrogen would most likely cause the peaks to shift towards lower frequencies and increase impedance values as described also by Moussaoui H. et al. [33] in the study of the online diagnosis tool of lab-scale SOFC.

To further ensure full reliability of the proposed association of the peaks, two additional tests were performed using geometrically altered cells. All other constituents of the cells remained identical, including the thickness of the AFL. The results of the comparative study of two cells with thickness of the anode, respectively, 300 and 400 µm are presented in Fig. 4. As can be seen in the DRT spectra, clear change occurred exclusively in the P2 process. This is predominantly a direct proof that P2 is related to the diffusion process in Ni-YSZ cermet. The effect might be counterintuitive as the depression of the impedance as well as the shift towards higher frequency was observed for a higher thickness of the anode. In fact, the 400 µm anode is more porous than thinner one. This is due to the technological aspects of cell processing. The difference in porosity was first discovered via SEM imaging and later measured via Archimedes principle porosity measurement using kerosene as the penetrating liquid. The values of the apparent porosity and SEM micrographs can be seen in Fig. 4. (right). Higher porosity, followed by a rounder shape of the pores, and better interconnectivity between them led to a depression of the polarization resistance from mass transport through the anode (P2). All other peaks were minorly affected by the change in anode thickness.

A similar study was performed for the cathode side to check which of the processes can be directly bound to the mass transport through the LSC layer. The tests were performed using a commercial test rig, and the button cells were prepared as previously described. The results are

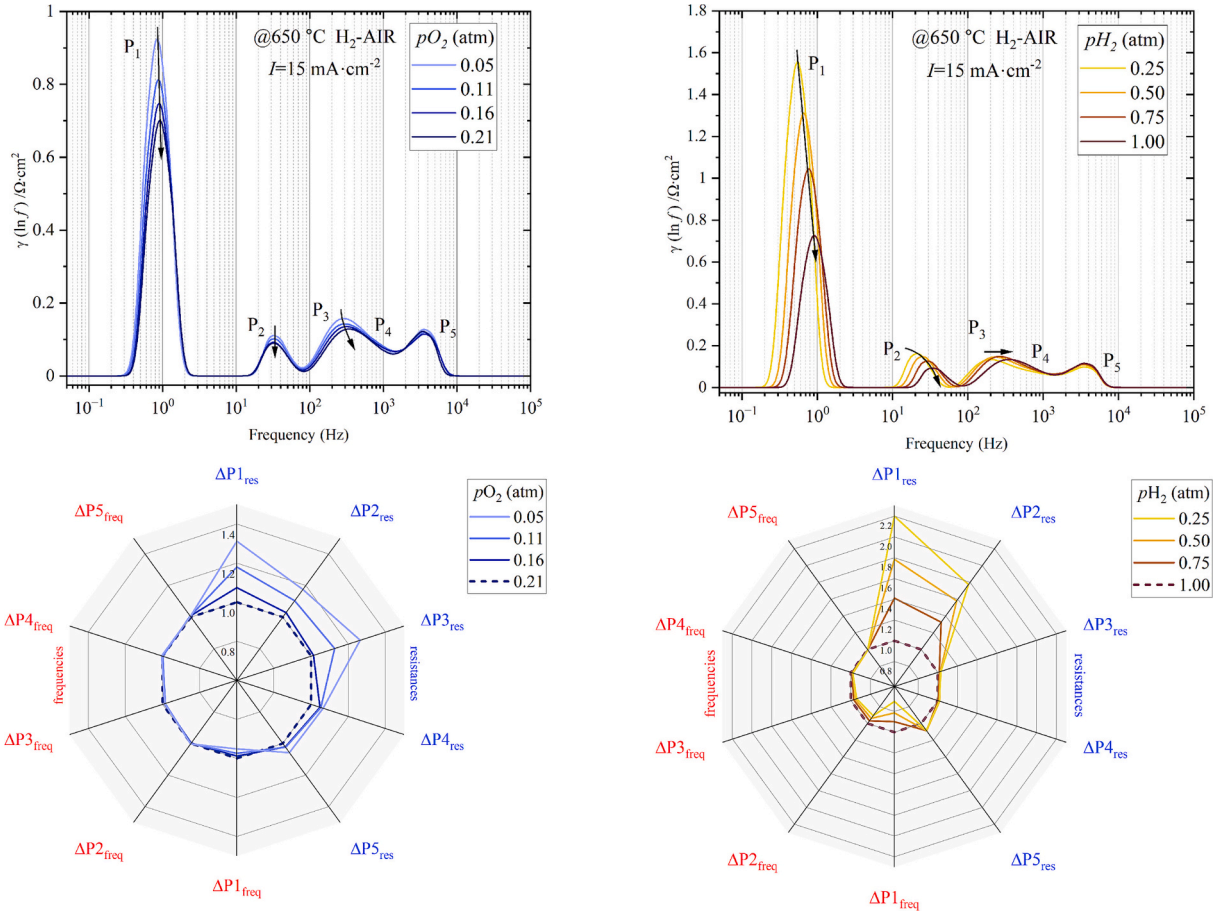

Fig. 3. DRT spectra of the single cell under various pO_2 conditions on the cathode (left) and changing pH_2 conditions on the anode (right) with corresponding changes depicted in spider graphs.

Table 4
Results of the CNLS fitting on two extreme conditions of pO_2 or pH_2 change with relative change of each resistance (rounded up to full %).

Parameter/ Unit	Value	Rs (mΩ)	Rpol (mΩ)	P1 (mΩ)	P2 (mΩ)	P3 (mΩ)	P4 (mΩ)	P5 (mΩ)
pO_2 (atm)	0.21	0.53	13.18	6.55	0.89	3.84	0.73	1.17
pO_2 (atm)	0.05	0.57	16.15	8.62	1.09	4.52	0.68	1.24
ΔR_i (%)			23	32	22	18	−7	6
pH_2 (atm)	1	0.53	13.25	6.66	0.87	3.82	0.67	1.21
pH_2 (atm)	0.25	0.52	21.48	14.57	1.54	3.86	0.58	0.93
ΔRi (%)			62	119	77	1	−13	−23

presented in Fig. S3. in Supplementary Materials. According to changes in DRT spectra measured for the cell with 20 and 40 μm cathode, the most affected peak was P3, which is located within a frequency range similar to P3 of the pristine large cell. The highest increase in the area revealed that P3 is directly related to cathodic processes. Zheng Z. et al. [34] studied impregnated cathodes, where a similar behavior of the peaks responsible for diffusion and charge transfer was observed after alteration of the microstructure of the LSC-CGO20 composite. It can also be seen that the overall impedance of the charge transfer processes decreases as the thickness of the cathode increases. An identical trend was observed by Barbucci A. et al. [35], where they have shown remarkable influence of LSM thickness on the reaction rates. They described the dependence between the added electrode volume, resulting in more active sites for oxygen reduction, and the progressive drop of efficiency due to mass transport losses in thicker layers of LSM. The observations of the button cell resulted in another valuable piece of information proving the way the peaks were ascribed to the physicochemical processes is correct.

Additionally, the aforementioned P6 process could be observed more clearly in the button cell DRT analysis due to a higher overall impedance. It is highlighted in Fig. S6. and as it corresponds to the transport of the ionic species in the cathode, it also reacts to some extent to the change in LSC thickness.

3.5. Influence of the water vapor partial pressure on DRT spectra

To bring the ADIS closer to the realistic conditions under which the cell is operating, but without the need to draw much current, a series of tests under various pH_2O and various temperature under $pH_2O = 0.375$ were performed. The results are shown in Fig. 5A-B and Fig. 5C-D, respectively. For various water vapor measurements, the temperature was decreased to 600 °C due to a severe decrease in impedance followed by an impeded DRT analysis. The DRT spectrum from the test with pure hydrogen taken at 600 °C was given for comparison in Fig. 5A. The addition of water vapor had a significant influence on the polarization resistance of the cell. Series and polarization resistances of the pure hydrogen fed cell ($pH_2O = \sim 0$) and the cell with a water concentration of 50 vol% ($pH_2O = 0.5$) decreased by 30 % and 70 %, respectively. This is mostly due to the pronounced drop in the gas conversion resistance, which is in line with the Nernst potential change caused by the introduction of water. As predicted in Fig. S5. an increase in pH_2O causes a sudden decrease in the Nernst resistance followed by an increase above $pH_2O = 0.5$ (P1, Fig. 5A). Furthermore, the P1 process appeared to be nearly non-responsive when temperature increased in the presence of 37.5 vol% H_2O (Fig. 6C). This further proves that P1 is related to gas conversion resistance.

Under the influence of water vapor, the overall polarization resistance decreased strongly. It is best seen for the P3 and P4 processes, where the addition of steam caused a total overlap of those two. The higher share of the peak located at $\sim 10^3$ Hz corresponds to the charge transfer overpotential (P4), which is directly influenced by water vapor as was previously stated by Budiman R.A. et al. [36]. During their study, hydrogen oxidation reaction (HOR) mechanisms in Ni/YSZ porous anodes were examined via EIS measurements and transmission line model calculations. It was found that humidity increases the surface catalytic activity and changes the rate-limiting steps of HOR, which, in the end, decreases the polarization resistance of the charge-transfer reaction. Furthermore, the merging, depression, and shift in the frequency of P3/P4 processes is directly connected to the mass transport mechanism through the active zone of the cell, where most of the overpotentials are generated. According to the non-linear Butler-Volmer expression model of Qiangqiang L. et al. [37], it was numerically shown that a decrease in the share of the H_2 molar fraction increases the reaction rate. Similar observations were made by Del Zotto L. et al. [38], where diffusion-related peaks in DRT revealed a shift towards higher frequencies when pH_2 was lowered. This again is in line with the results obtained in this study and presented in Fig. 5A.

Similarly to P1, the diffusion resistance of the anode bulk (P2) changed when water vapor was introduced. The mass transport of H_2O-H_2 through Ni/YSZ depends not only on the geometric factors but also on the chemical potential and the rates of reactions that occur at active sites on the electrode. In this sense, the diffusive part of the impedance

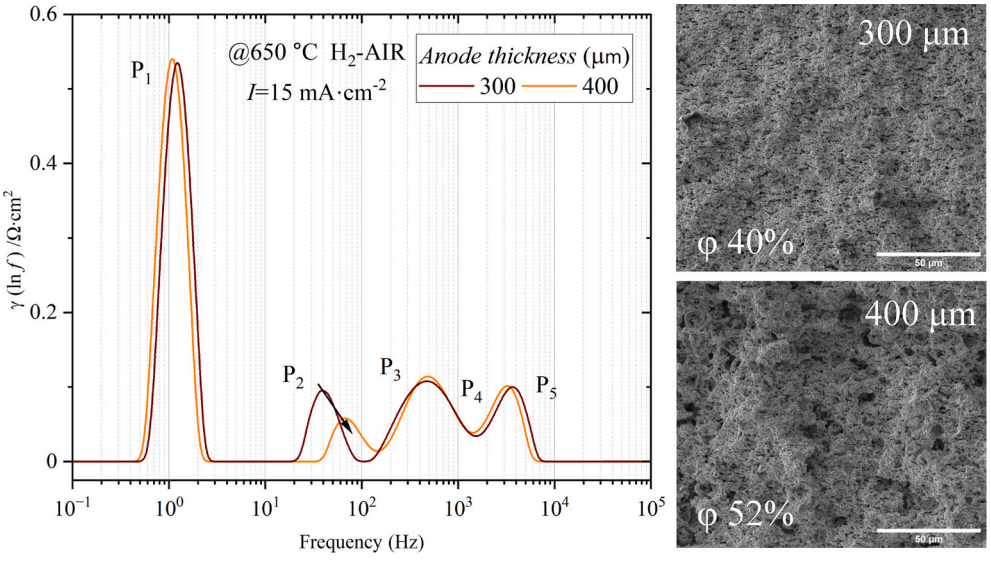

Fig. 4. DRT spectra of the single cell with various thickness of the anode with corresponding SEM fractures. Scale bar is 50 μm. The apparent porosities were given in the micrographs.

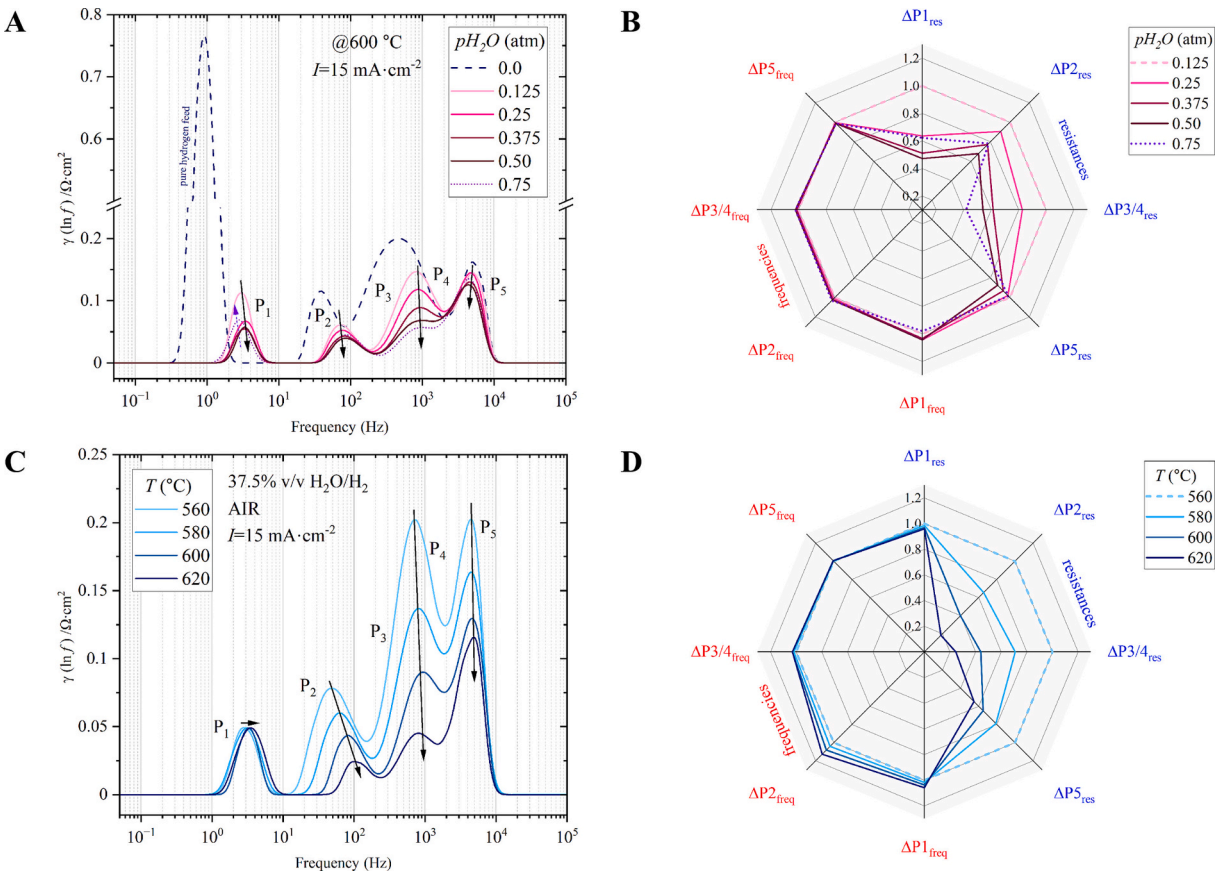

Fig. 5. DRT spectra of the single cell under various pH_2O on the anode (A) and changing cell temperature under constant $pH_2O = 0.375$ (C) with corresponding changes depicted in spider graphs (B,D).

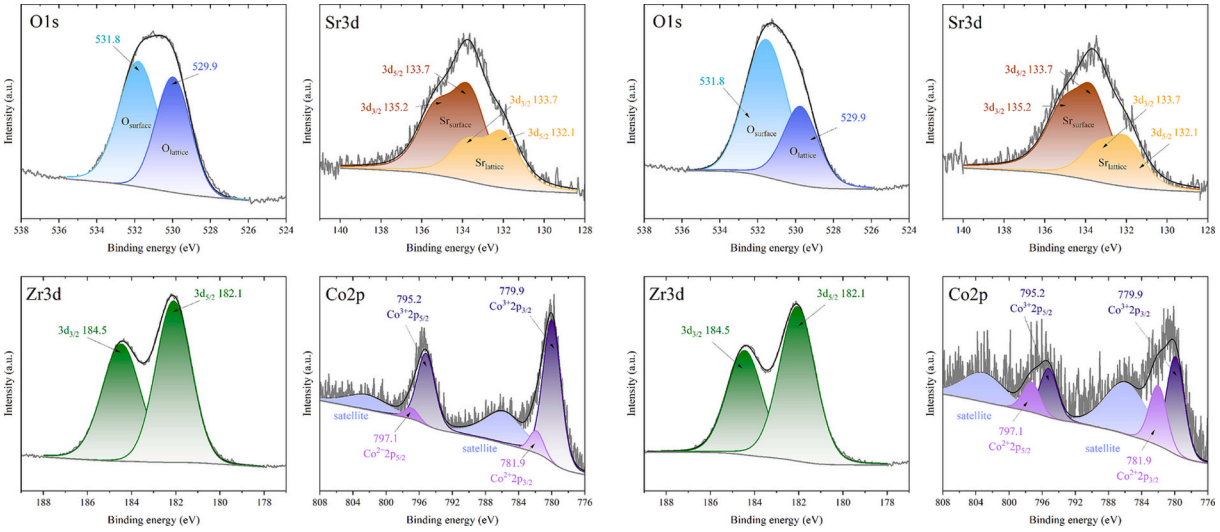

Fig. 6. XPS spectra of the Sr3d, Zr3d, Co2p, and O1s core levels of powdered cell before and after the operation.

can be linked to the processes P1 and P4, which have been highly influenced by water vapor. On the one hand, the higher the exchange rate, the higher the limiting current and the turnover frequency. Together, it affects the diffusion rate of the reactants and products [29]. It was also stated before that the diffusion constant of the H_2O-H_2 mixtures is non-constant and depends on the gas mixing ratio [27]. On the other hand, depending on the conditions, above some steam concentration, the diffusion becomes highly limited because of more sluggish water diffusion rates compared to much smaller hydrogen molecules. Furthermore, the Nernst potential is directly bound to the diffusion processes (P1). After the sudden drop in low steam concentration, the resistance rises again above $pH_2O \sim 0.5$ (see Fig. S5.). Overall, the altogether effects can be observed as nonrestricted depression of the P4 process when increasing the pH_2O, while the peak P2 revealed regrowth at a higher steam concentration.

Process P5 was minorly dependent on water vapor concentration, as

seen in Fig. 5B. It was previously described by Sakai N. et al. [39] that the addition of the steam to the surrounding of YSZ was beneficial in terms of interfacial ionic conductivity. However, if the water concentration was drastically increased and long-term measurements were performed, the conductivity of the electrode was diminished due to the blocking effect of water molecules and/or hydroxyl groups followed by enhanced degradation. Similar effects were observed in this study. In that sense, one can see that the P5 peak is mostly related to the YSZ ionic conductivity. The observations made on the influence of steam on the placement of DRT peaks follow the work of Kullman F. et al. [40] where various scenarios of the fitting of advanced transmission models were introduced in GDC-Ni cells.

The summary of various findings on the assignment of the DRT peaks is given in Table 5. along with the ascription of the processes in the SOFCs obtained in this work.

The description of the origin of the DRT peaks obtained in this study is partially consistent with the findings published in different works. The main similarity falls within the 1–10 and > 1 k Hz ranges, where many other groups assigned those peaks to gas conversion and YSZ ionic conductivity, respectively. The rest of the peaks were attributed to slightly different processes. For 10–100 Hz peaks, it was found with a high dose of confidence that the resistance comes from anode support layer diffusion. In contrast, for other authors, there is either less agreement on the assignment of the corresponding processes or the assumptions are made for a very broad frequency range. In general, the presence of interchanging variables that can affect the resistances of either of the electrodes makes separation of contributions an extremely challenging task. While it is natural to assign DRT peaks to specific electrodes, one should call attention that different electrodes may contribute to different peaks at the same time.

3.6. Post-mortem characterization of the single cell

Prior to testing regime, the cell was initially characterized by XRD, SEM, and XPS methods. The phase composition before the tests was measured and the results are shown in Fig. S6. in Supplementary Materials along with the SEM image taken from the cross-section of a freshly reduced cell. The anode was composed of YSZ and metallic Ni grains with a trace of ZrO_2 being a common impurity in the YSZ stock powder as well as a small amount of NiO, which formed during the transportation and storage of the cell under ambient conditions before diffractograms were taken. On the cathode side the major peaks were attributed to cubic LSC64 (*Pm-3m*), with the minor peaks of the 8YSZ and the CGO coming from underneath the cathode layer.

Collected XPS spectra of Sr3d, Zr3d, Co2p, and O1s from the pristine reduced sample were deconvoluted and the results are given in Fig. 6. The $Zr3d_{5/2}$-$Zr3d_{3/2}$ doublet was located at 182.1 and 184.5 eV, respectively. Based on that it was proved that all the zirconium remained in the Zr^{4+} state in the form of reduction resistant 8YSZ ionic component of the cermet material [41,42]. The measurement gave rise to the peaks attributed to the cathode material LSC64 in the form of two Sr3d doublets located at 132.1–133.7 and 133.7–135.2 eV, respectively. In general, those were attributed to the coexistence of Sr ions embedded within the perovskite lattice of the perovskite (lower energy) and the surficial species mainly involving the thin layer of terminal SrO and $SrCO_3$ (at higher binding energy). This is in line with the general behavior of the $(La,Sr)CoO_3$ compound, as it tends to create the segregations of the Sr oxides on the surface. The segregated Sr ions upon contact with ambient air form the carbonate. It is a generally known behavior and it is not considered a cause of lowering performance based on the study of Pagliari M. et al. [43]. The O1s peaks found at 529.9 and 531.8 eV have implied an equal share of surface and lattice oxygen in the freshly reduced sample [44,45]. Despite that, one must remember that the O1s signal is a superposition of many coming from both the cathode and anode side, as well as carbon tape used for mounting. The Co2p core level spectrum was decomposed into two major doublets corresponding to Co^{2+} and Co^{3+} states with the $Co2p_{3/2}$ peaks located at 779.9 and 781.9 eV, respectively [46–48]. A much higher share of the Co^{3+} state of cobalt ions increased the overall valence state of the metal to ~2.9 (based on the peak integrated area). A higher Co^{3+}/Co^{2+} ratio promotes the charge transfer reactions and is generally considered a positive aspect of the electrode material [49,50]. On the other hand, the high valence of the transition metal at the B site of the perovskite can be considered as a major mechanism of charge compensation and reduces the concentration of oxygen vacancies that provides efficient ionic conductivity [51,52]. It is one of the reasons for the utilization of LSCF or LSCF-CGO composites in the most recent cells.

After 1700 h, the cell was cooled and subjected to a similar

Table 5
Attribution of DRT peaks to the processes obtained in this study and by different authors under varying working conditions.

Frequency (Hz)					Ref.
0.2–20	10–100	20–2000	1-10 k	50 k	[5]
Cathode gas diffusion and anode gas diffusion	Cathode and anode electrochemical reactions (charge transfer) and anode gas diffusion	Cathode and anode electrochemical reactions (charge transfer)	Ion transport in anode	Ion transport in cathode	
0.1–1	1–1000	1–1000	100–1000	1-10 k	[11]
Gas diffusion in the air electrode structure	Oxygen surface exchange kinetics and O^{2-} diffusivity in the bulk of the air electrode	Gas diffusion in the fuel electrode substrate	Gas diffusion coupled with charge transfer reaction and ionic transport (fuel electrode functional layer)		
0.1–20	2–200	20–1000	0.1–10 k	10-100 k	[26]
Gas diffusion process at the anode substrate	Oxygen surface exchange and diffusion processes at the cathode	Steam production process at the anode	Charge transfer and ionic conduction processes at the anode	Ionic conduction process at the interface between the electrolyte and the mixed ionic-electronic conductor (MIEC) of the cathode	
<1	1–10	10–100	100–500	500-100 k	[16]
Conversion diffusion at low pO_2 transport in reforming mixture	Gas conversion	Fuel electrode diffusion/ oxygen electrode reaction + solid state diffusion	Secondary peaks (fuel and oxygen electrode transport)	Fuel electrode charge transfer	
0.1–1	~1	1–10	100–1000	>1 k	[28]
N/A	Gas conversion	Inhibited gas diffusion within the Ni/YSZ anode substrate	Activation polarization at the cathode	Gas diffusion coupled with charge transfer reactions at TPB and ionic transport in the anode functional layer	
<1	1–10	10–100	100–1000	>1 k	This work
(in stacks) gas transfer resistance in the interconnect	Gas conversion	Diffusion of the gas in the anode bulk	Mass transport across AFL/ cathode and charge transfer reactions at the anode	YSZ (3−10*k*) and LSC (~40 k) ionic conduction	

characterization scheme as before the testing. The results are also presented in Fig. 6 (right). Excluding the almost unaffected Zr3d spectrum, clear evidence of chemical changes was observed. In the case of O1s core level, an increase in the share of surface oxygen was noticed. This can be to some extent connected to the increase in the amount of formed surficial SrO and Co_xO_y. It is proved by a slight increase in the concentration of surficial Sr as seen in the Sr3d deconvoluted spectrum after the test. Furthermore, a noticeable change in the Co^{2+}/Co^{3+} ratio is visible. As shown in Fig. S7., XRD studies on the spent cell revealed the formation of a Co_3O_4-like phase in the air electrode layer. This is a fairly common behavior of LSC64 [53] and, in general, it may stabilize the structure and can be beneficial to the catalytic activity of the compound [54]. In general, an increase in the relative concentration of Co^{2+} (781.9–797.1 eV) in the Co2p core level spectrum is obvious. No obvious shift in doublet placement was observed, although a slight broadening of the doublets is visible. It was calculated, that the average oxidation state of Co cations decreased from ~2.9 to ~2.6 what is quite a common behavior of the LSC perovskite and may cause a decrease in the number of oxygen vacancies [55]. Despite that, chemical changes in LSC64 can hardly be considered a cause of performance drop. In summary, XPS studies indicated chemical changes in the composition of the cell at the material level.

During long-term exposure, the cell underwent a slight change in the distribution of the peaks of the electrochemical processes according to the DRT spectra taken after conditioning and at the terminal point visible in Fig. 7. All processes besides the gas conversion (P1) were slightly affected during the testing time. Due to the reorganization of the Ni grains, the diffusion-related peak (P2) decreased and shifted towards higher frequencies, indicating easier transport of the mass across the anode. The development of the porosity can also be seen in Fig. 7. as an elemental map of the Ni—Zr distribution. The complementary SEM image of the dismounted cell is shown in Fig. S7. in Supplementary Materials. It is visible that Ni grains increase in size, and the previously finer structure becomes coarser with a higher share of open porosity. The influence of Ni-YSZ coarsening on conductivity and microstructural changes was previously studied by our group [56]. The cermet was prepared via a novel soft-hard templating method, and inhibition of the conductivity loss was obtained as a result of the nanostructuring. Despite enhancing mass transport, the agglomeration of Ni in the lattice leads to the formation of isolated metallic islands, which decreases the length of the triple phase boundary (TPB) and breaks the conduction paths. A similar conclusion can be drawn looking at the measurements of the specific surface area (SSA) via the N_2 sorption technique (BET isotherm). The freshly reduced and spent cells had the SSA value of 1.96 ± 0.11 $m^2 \cdot g^{-1}$ and 2.36 ± 0.12 $m^2 \cdot g^{-1}$, respectively, with the majority of active surface coming from the macroporosity of the anode base layer. The increase in total pore volume was also observed from 5.24 to 6.74 $\times$ 10^{-3} $cc \cdot g^{-1}$, indicating the coarsening of the structure that enhances the diffusion of gases through the cermet [57]. Despite the overlap of the P3 and P4 peaks, it seems that the P4 peak corresponding to the charge transfer reactions decreased and shifted towards lower frequencies. It is in line with the change in the density of the active sites for the reactions while the Ni lattice reorganization progresses.

As seen in the elemental maps in Fig. 7., minor segregation of Co_xO_y species occurred within the cathode material, but the influence on degradation is rather negligible at that state [44]. However, the existence of Co-enriched grains implied the diffusion of Sr ions across the electrode [58]. On the Sr distribution map, it is clearly visible that Sr diffused through the cathode towards the YSZ/GDC interface forming the secondary phase, which was confirmed by XRD studies on the spent

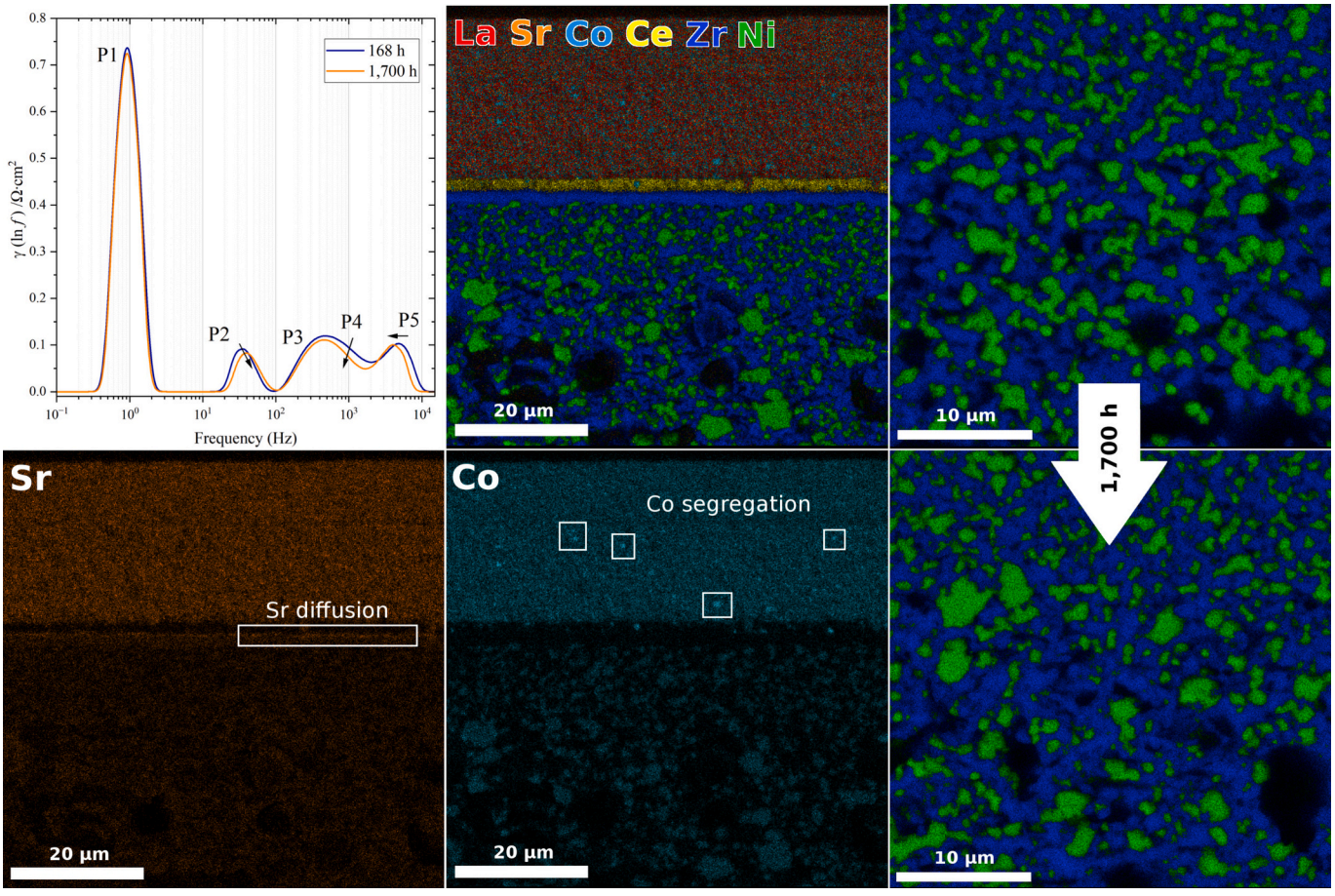

Fig. 7. DRT spectra of conditioned and spent cell with EDX distribution maps of selected elements.

cell. The diffractogram revealed a minor formation of poorly conducting $SrZrO_3$ (Fig. S7.). This is a fairly common behavior that was previously reported for LSC-based cathodes. The formation of $SrZrO_3$ is strongly influenced by the quality of the GDC grains that form the barrier layer, as described by Chou et al. [59]. Based on their work, the porous structure of the ceria layer in the tested cell led to an enhanced inter-diffusion and the formation of the Sr-Zr-O phase, which caused retention of the conduction paths for oxygen ions and an increase in the ohmic resistance. Although SrO termination may not deteriorate the performance of the cathode [60], the formation of $SrZrO_3$ led to an overall increase in the R_s value and a shift of the peak of the P5 process towards lower frequencies. Despite that, the amount was rather low and apparently did not strongly influence the efficiency of the cell during the test time. Cell degradation caused by the decrease in the number of percolating Ni grains and the formation of $SrZrO_3$-like insulating phases was compensated by a strong decrease in the polarization resistance. Therefore, the overall performance of the cell improved during the testing time. It can be stated that the DRT methodology helps to understand the possible sources of the degradation prior to materials postmortem characterization. In summary, the cell followed the most common regime of material deterioration, which was the coarsening of the anode and the formation of $SrZrO_3$ on the electrolyte. These issues should be addressed when improving the design of the next generation of cells.

3.7. Performance of the selected cells in the stack

The previous findings achieved using the measurements of the single cell gave rise to valuable conclusions regarding the overpotentials of the electrochemical processes, but the aim of this study was to find a tool to characterize the performance of the stack in a cell-by-cell manner. The assignment of the peaks to the corresponding processes and finding real causes of the changes in the DRT spectra based on single-cell measurements allowed one to find the 'fingerprint' of the cells. Based on that, it was possible to measure the individual cells in the stack one by one, determine their actual performance, and identify issues that lead to the deterioration of stack efficiency. To validate this approach, a series of data was collected for the 15-cell operating stack with respect to cells No. 5 and No. 8 being placed closer to the bottom of the stack and in the middle, respectively. EIS spectra were collected after stabilization of stack performance (T1) and after around two weeks of undisturbed work (T2). The results of the DRT analysis with the corresponding EIS spectra are presented in Fig. 8A-B. To better compare both the Nyquist and DRT spectra, the frequency scale in the DRT plot was reversed. Furthermore, a comparative graph of the results of the single cell and stack (at T2 point) is included in Fig. 8C.

It is clearly visible that the distribution of the peaks obtained from the stack follows the one described for the single cell. The peak summit frequencies are in line with previous findings. Two major differences were identified for stack spectra. A new peak appeared at $\sim 10^{-1}$ Hz, one order of magnitude lower in frequency than the gas conversion P1 peak (Fig. 8C.). Due to the existence of interconnect plates and the lower rate of air feed to the stack compared to the single cell, the appearing peak could be related to the cathode side interconnector channels diffusion resistance. In the case of single-cell measurements, the mass transport processes of the air to the cathode layer do not bring any visible contribution to the overall polarization resistance, because of the simplified geometry of the measuring housing and direct feeding of the air at high rates. This low frequency peak will be further studied and described in our upcoming papers. Other than that, the DRT spectra of the cells from two different places in the stack are of similar distribution. Comparing the spectra from Fig. 8A-B. one can see that the cells differ slightly, especially regarding the P2 diffusive process. The higher depression of the P2 peak in Cell No.8 came from the fact that the cell was placed in the middle part of the stack. Due to the generation of heat in SOFC mode and its worse dissipation in the middle part of the stack,

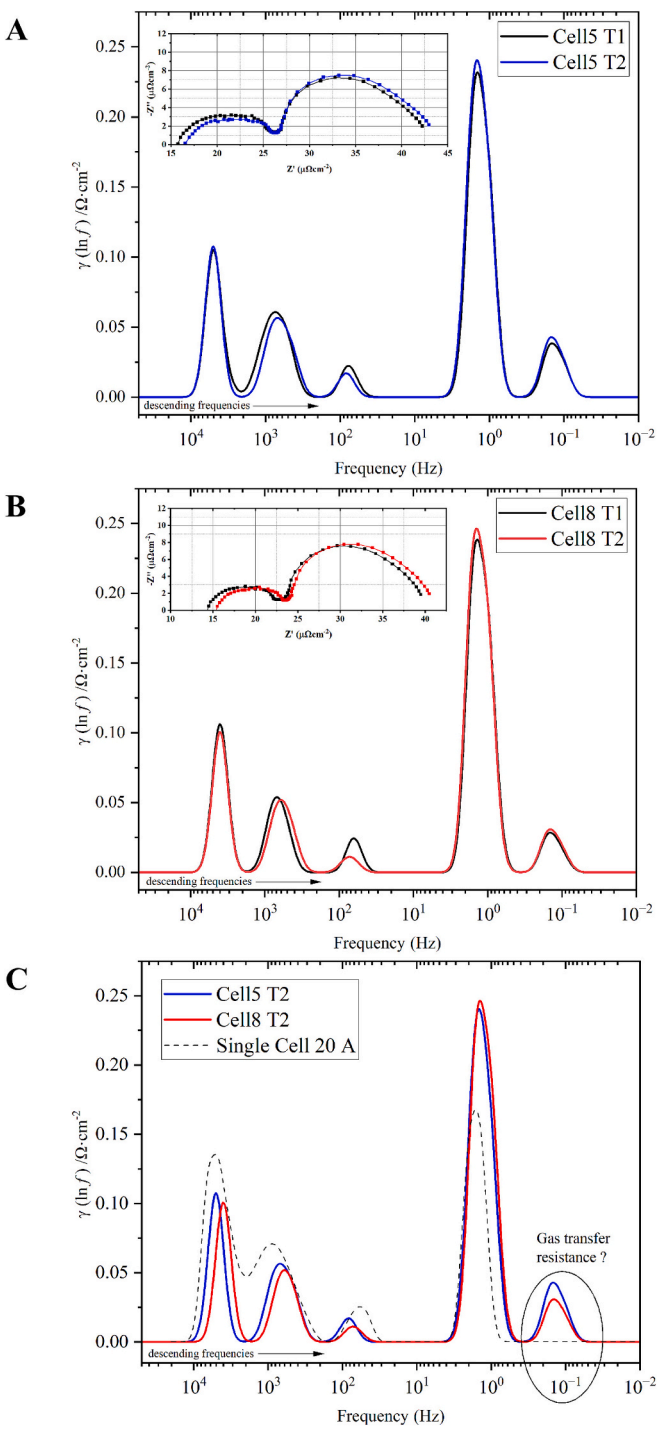

Fig. 8. DRT spectra of the cells No. 5 and No. 8 at two different time points (A-B) and (C) comparison of the single cell results and stack-derived data.

Cell No. 8 is held at slightly higher temperature than the rest of the cells. Therefore, it is visible that even a minor increase in the operating temperature had an influence on the reorganization of the Ni-YSZ microstructure. In that sense, it is predicted that Ni agglomeration and opening porosity in Cell No. 8 were much stronger than for another cell tested, due to thermally activated diffusion of the Ni species within the Ni-YSZ electrode. In both cases, the change in Nyquist plots was visible, due to the increase in the series resistance caused by either coarsening of the microstructure and loss of conductivity or the formation of the $SrZrO_3$ phase, which was also found after the tests using the single cell. The higher drop in the performance of Cell No. 8 is also visible in the

voltage data collected during the long-term operation presented in Fig. S8. in Supplementary Materials.

The results clearly indicated the possibilities for the use of EIS spectra for the description of the actual state of the single cells in the stack. After the construction of the database with the 'fingerprints' of various types of single cells, it could be possible to further develop an automatic tool for in situ monitoring of the performance of the stack. Using AI and more complex algorithms, it is more than possible to create a system for control of the actual parameters, recognition of performance problems, and automatic mitigation of stack degradation.

4. Conclusions

To better understand the processes occurring inside the SOCs, a series of measurements was performed using a large-scale single cell to further introduce the findings into stack characterization. This approach was chosen to omit laborious work when trying to perform a similar analysis using actual cells included in the operating stack. The cells were examined by means of EIS and analyzed using DRT-ADIS methodologies. The major improvement was the shift to real-life cells, which pointed out the differences in the common concepts of electrochemical characterization compared to the baseline scenarios mainly involving button cells and idealized conditions of measurements that may lead to oversimplified conclusions. This study provides a nuanced understanding of SOC behavior that goes beyond what many reports on button cells have to offer.

In general, single cell tests revealed the existence of five major peaks in the DRT spectra. Additionally, the sixth process was determined to be related to the ionic transport on the cathode side, but because of the high inductance of the housing, it was removed from further fitting to exclude possible errors. The rest of the processes were ascribed to the corresponding electrochemical or mass transfer processes in SOC based on differences in the DRT spectra when specific working conditions were altered. Based on the DRT analysis, it was possible to deconvolute and quantify the resistance resulting from the specific processes that contribute to the overall polarization losses in the cell.

The single cell was subjected to 1700 h of operation and based on postmortem analysis it was possible to determine the main issues when it comes to degradation. The most relevant processes were the microstructure coarsening in the anode via Ni agglomeration and the diffusion of Sr and Co cations towards the electrolyte and within the electrode layer. Similar observations were made when using the 'electrochemical fingerprint' of a single cell in stack tests. A clear indication of the differences in the degradation mechanisms was provided based on the DRT spectra of two various cells at two distinct places in the stack. As a result of the thermal gradients and hotspots, inner cells suffer more from microstructure reorganization as well as electrolyte poisoning.

The results of this study help to understand and minimize the degradation of SOC stacks, thus promoting this technology for efficient and cost-effective hydrogen applications. To do so, the future study will involve standardization of the characterization methodology of large-scale cells using various cells widely used for stack construction to further confirm the viability of the approach and build the foundation for the database of 'electrochemical fingerprints'. More effort will be made to bring the measurement conditions closer to the actual working environment of the cells regarding the higher steam content and influence of the interconnect plates. This will underscore the importance of evolving methodologies to better capture the complexities of electrochemical systems.

This approach could be a promising prelude to the development of the autonomous tool for in situ control of the actual state of stack cells connected to possible degradation mitigation response systems during long-term test runs, as well as quality control algorithms determining the influence of novel materials used in the cells on overall performance change.

CRediT authorship contribution statement

Patryk Błaszczak: Writing – review & editing, Writing – original draft, Methodology, Investigation, Data curation, Conceptualization. **Pyry Mäkinen:** Writing – original draft, Investigation, Data curation. **Aleksander Mroziński:** Investigation, Formal analysis, Data curation. **Agata Ducka:** Writing – original draft, Investigation, Formal analysis. **Grzegorz Jasiński:** Writing – original draft, Software. **Olli Himanen:** Supervision, Resources. **Piotr Jasiński:** Writing – original draft, Supervision, Resources, Methodology, Formal analysis.

Declaration of competing interest

The authors declare the following financial interests/personal relationships which may be considered as potential competing interests: Piotr Jasinski reports financial support was provided by National Science Centre Poland. If there are other authors, they declare that they have no known competing financial interests or personal relationships that could have appeared to influence the work reported in this paper.

Acknowledgements

This work was supported by a project OPUS22 funded by National Science Centre Poland, based on decision UMO-2021/43/B/ST8/01831. This research was supported by NAWA – Polish National Agency for Academic Exchange, grant number BPN/BEK/2022/1/00204. The authors would like to thank the team of Markku Santala, Werneri Huhtinen, and Santeri Saxelin for assuring proper work of moody SOC testing station very much needed to accomplish the publication. We would like to acknowledge Elcogen for supplying us with the cells for testing and Antonio Alfano for supporting this work with his valuable comments.

Appendix A. Supplementary data

Supplementary data to this article can be found online at https://doi.org/10.1016/j.apenergy.2025.125983.

Data availability

Data will be made available on request.

References

[1] Xu Q, Guo Z, Xia L, He Q, Li Z, Temitope Bello I, et al. A comprehensive review of solid oxide fuel cells operating on various promising alternative fuels. Energy Convers Manag 2022;253. https://doi.org/10.1016/j.enconman.2021.115175.
[2] Hubert M, Laurencin J, Cloetens P, Morel B, Montinaro D, Lefebvre-Joud F. Impact of nickel agglomeration on solid oxide cell operated in fuel cell and electrolysis modes. J Power Sources 2018;397:240–51. https://doi.org/10.1016/j.jpowsour.2018.06.097.
[3] Sreedhar I, Agarwal B, Goyal P, Singh SA. Recent advances in material and performance aspects of solid oxide fuel cells. J Electroanal Chem 2019;848:113315. https://doi.org/10.1016/j.jelechem.2019.113315.
[4] McPhail SJ, Frangini S, Laurencin J, Effori E, Abaza A, Padinjarethil AK, et al. Addressing planar solid oxide cell degradation mechanisms: a critical review of selected components. Electrochem Sci Adv 2022;2. https://doi.org/10.1002/elsa.202100024.
[5] Wang Y, Marchetti B, Zhou XD. Call attention to using DRT and EIS to quantify the contributions of solid oxide cell components to the total impedance. Int J Hydrog Energy 2022;47:35437–48. https://doi.org/10.1016/j.ijhydene.2022.08.093.
[6] Zhang Y, Chen Y, Li M, Yan M, Ni M, Xia C. A high-precision approach to reconstruct distribution of relaxation times from electrochemical impedance spectroscopy. J Power Sources 2016;308:1–6. https://doi.org/10.1016/j.jpowsour.2016.01.067.
[7] Xia J, Wang C, Wang X, Bi L, Zhang Y. A perspective on DRT applications for the analysis of solid oxide cell electrodes. Electrochim Acta 2020;349. https://doi.org/10.1016/j.electacta.2020.136328.
[8] Ghamarinia M, Babaei A, Zamani C, Aslannejad H. Application of the distribution of relaxation time method in electrochemical analysis of the air electrodes in the SOFC/SOEC devices: a review. Chem Eng J Adv 2023;15. https://doi.org/10.1016/j.ceja.2023.100503.
[9] Bertei A, Ruiz-Trejo E, Tariq F, Yufit V, Atkinson A, Brandon NP. Validation of a physically-based solid oxide fuel cell anode model combining 3D tomography and

impedance spectroscopy. Int J Hydrog Energy 2016;41:22381–93. https://doi.org/10.1016/j.ijhydene.2016.09.100.
[10] Vafaeenezhad S, Hanifi AR, Laguna-Bercero MA, Etsell TH, Sarkar P. Microstructure and long-term stability of Ni-YSZ anode supported fuel cells: a review. Mater Futur 2022;1. https://doi.org/10.1088/2752-5724/ac88e7.
[11] Leonide A, Apel Y, Ivers-Tiffee E. SOFC modeling and parameter identification by means of impedance spectroscopy. ECS Trans 2009;19:81–109. https://doi.org/10.1149/1.3247567.
[12] Lyu Z, Li H, Han M, Sun Z, Sun K. Performance degradation analysis of solid oxide fuel cells using dynamic electrochemical impedance spectroscopy. J Power Sources 2022;538. https://doi.org/10.1016/j.jpowsour.2022.231569.
[13] Lazanas AC, Prodromidis MI. Electrochemical Impedance Spectroscopy—A Tutorial. ACS Meas Sci Au 2023;3:162–93. https://doi.org/10.1021/acsmeasuresciau.2c00070.
[14] Wan TH, Saccoccio M, Chen C, Ciucci F. Influence of the discretization methods on the distribution of relaxation times deconvolution: implementing radial basis functions with DRTtools. Electrochim Acta 2015;184:483–99. https://doi.org/10.1016/j.electacta.2015.09.097.
[15] Drasbæk D, Kungas R, Blennow P, Heiredal-Clausen T, Høgh JVT, Hauch A. A framework for characterizing commercial solid oxide electrolysis stacks using electrochemical impedance spectroscopy and equivalent circuit modeling. ECS Trans 2021;103:529–43. https://doi.org/10.1149/10301.0529ecst.
[16] Caliandro P, Nakajo A, Diethelm S, Van Herle J. Model-assisted identification of solid oxide cell elementary processes by electrochemical impedance spectroscopy measurements. J. Power Sources 2019;436. https://doi.org/10.1016/j.jpowsour.2019.226838.
[17] Zarabi Golkhatmi S, Asghar MI, Lund PD. A review on solid oxide fuel cell durability: latest progress, mechanisms, and study tools, renew. Sustain Energy Rev 2022;161. https://doi.org/10.1016/j.rser.2022.112339.
[18] Błaszczak P, Łapiński M, Wang S-F, Jasiński P, Bochentyn B. Exsolution of Ni nanoparticles on the surface of cerium and nickel co-doped lanthanum strontium titanate as a new anodic layer for DIR-SOFC. Anti-coking potential and H2S poisoning resistance of the prepared material. Int J Hydrog Energy 2020;45:29186–200. https://doi.org/10.1016/j.ijhydene.2020.07.162.
[19] Harrison CM, Slater PR, Steinberger-Wilckens R. A review of solid oxide fuel cell cathode materials with respect to their resistance to the effects of chromium poisoning. Solid State Ionics 2020;354. https://doi.org/10.1016/j.ssi.2020.115410.
[20] Peng J, Zhao D, Xu Y, Wu X, Li X. Comprehensive analysis of solid oxide fuel cell performance degradation mechanism, prediction, and optimization studies. Energies 2023;16. https://doi.org/10.3390/en16020788.
[21] Nuggehalli Sampathkumar S, Aubin P, Couturier K, Sun X, Sudireddy BR, Diethelm S, et al. Degradation study of a reversible solid oxide cell (rSOC) short stack using distribution of relaxation times (DRT) analysis. Int J Hydrog Energy 2022;47:10175–93. https://doi.org/10.1016/j.ijhydene.2022.01.104.
[22] Park BK, Barnett SA. Boosting solid oxide fuel cell performance: via electrolyte thickness reduction and cathode infiltration. J Mater Chem A 2020;8:11626–31. https://doi.org/10.1039/d0ta04280c.
[23] Li J, Fan L, Hou N, Zhao Y, Li Y. Solid oxide fuel cell with a spin-coated yttria stabilized zirconia/gadolinia doped ceria bi-layer electrolyte. RSC Adv 2022;12:13220–7. https://doi.org/10.1039/d2ra02035a.
[24] Liang F, Yang J, Zhao Y, Zhou Y, Yan Z, He J, et al. A review of thin film electrolytes fabricated by physical vapor deposition for solid oxide fuel cells. Int J Hydrog Energy 2022;47:36926–52. https://doi.org/10.1016/j.ijhydene.2022.08.237.
[25] Drasbæk DB, Blennow P, Heiredal-Clausen T, Rass-Hansen J, Perin G, Høgh JVT, et al. Exploring electrochemical impedance spectroscopy to identify and quantify degradation in commercial solid oxide electrolysis stacks. Fuel Cells 2023. https://doi.org/10.1002/fuce.202300023.
[26] Sumi H, Shimada H, Yamaguchi Y, Nomura K, Sato K. Why is the performance different between small- and large-scale SOFCs? Electrochim Acta 2023;443:141965. https://doi.org/10.1016/j.electacta.2023.141965.
[27] He W, Yoon KJ, Eriksen RS, Gopalan S, Basu SN, Pal UB. Measurement of H 2 -H 2 O Effective Binary Diffusivity in Porous Anode of Solid Oxide Fuel Cells (SOFCs). ECS Meet Abstr 2009;MA2009-02:1327. https://doi.org/10.1149/ma2009-02/12/1327.
[28] Sun X, Hendriksen PV, Mogensen MB, Chen M. Degradation in solid oxide electrolysis cells during long term testing. Fuel Cells 2019;19:740–7. https://doi.org/10.1002/fuce.201900081.
[29] Nenning A, Bischof C, Fleig J, Bram M, Opitz AK. The relation of microstructure, materials properties and impedance of SOFC electrodes: a case study of Ni/GDC anodes. Energies 2020;13:5–9. https://doi.org/10.3390/en13040987.
[30] Osinkin DA. Detailed analysis of electrochemical behavior of high–performance solid oxide fuel cell using DRT technique. J Power Sources 2022;527:231120. https://doi.org/10.1016/j.jpowsour.2022.231120.
[31] Wang Y, Lyu Z, Li H, Han M, Sun K. Analysis of polarization characteristics and optimal operating conditions for industrial-sized SOFC based on comparison with button cells. Int J Hydrog Energy 2024;50:1308–23. https://doi.org/10.1016/j.ijhydene.2023.06.277.
[32] Jensen MB, Hauch SH, Sun A, Chen X, Ebbesen M, Mogensen SD. Diffusion rates of reactants and components in solid oxide cells, in: Proc. 13th Eur. SOFC SOE Forum 2018. Artic B1208 Eur Fuel Cell Forum AG 2018:71–82.
[33] Moussaoui H, Hammerschmid G, Van Herle J, Subotić V. Fast online diagnosis for solid oxide fuel cells: optimisation of total harmonic distortion tool for real-system application and reactants starvation identification. J Power Sources 2023;556:232352. https://doi.org/10.1016/j.jpowsour.2022.232352.
[34] Zheng Z, Jing J, Lei Z, Wang Z, Yang Z, Jin C, et al. Performance and DRT analysis of infiltrated functional cathode based on the anode supported SOFCs with long-term stability. Int J Hydrog Energy 2022;47:18139–47. https://doi.org/10.1016/j.ijhydene.2022.03.289.
[35] Barbucci A, Carpanese M, Reverberi AP, Cerisola G, Blanes M, Cabot PL, et al. Influence of electrode thickness on the performance of composite electrodes for SOFC. J Appl Electrochem 2008;38:939–45. https://doi.org/10.1007/s10800-008-9500-z.
[36] Budiman RA, Ishiyama T, Bagarinao KD, Kishimoto H, Yamaji K, Horita T. Dependence of hydrogen oxidation reaction on water vapor in anode-supported solid oxide fuel cells. Solid State Ionics 2021;362. https://doi.org/10.1016/j.ssi.2021.115565.
[37] Li Q, Li G. Modeling of the solid oxide fuel cell anode based on a new analytical model using nonlinear Butler-Volmer expression. Ionics (Kiel) 2021;27:3063–76. https://doi.org/10.1007/s11581-021-04079-w.
[38] Del Zotto L, Tamburrano G, Dell'Era A, Hatunoglu A, Ciro E. Determination and validation of polarization losses parameters to predict current/voltage-characteristics for SOFC button cell. Energy Convers Manag 2024;299:117877. https://doi.org/10.1016/j.enconman.2023.117877.
[39] Sakai N, Yamaji K, Horita T, Xiong YP, Kishimoto H, Brito ME, et al. Effect of water on electrochemical oxygen reduction at the interface between fluorite-type oxide-ion conductors and various types of electrodes. Solid State Ionics 2004;174:103–9. https://doi.org/10.1016/j.ssi.2004.07.027.
[40] Kullmann F, Mueller M, Lindner A, Dierickx S, Mueller E, Weber A. DRT analysis and transmission line modeling of ceria based electrodes for solid oxide cells. J Power Sources 2023;587:233706. https://doi.org/10.1016/j.jpowsour.2023.233706.
[41] Bulavchenko OA, Vinokurov ZS, Afonasenko TN, Tsyrul'Nikov PG, Tsybulya SV, Saraev AA, et al. Reduction of mixed Mn-Zr oxides: in situ XPS and XRD studies. Dalt. Trans. 2015;44:15499–507. https://doi.org/10.1039/c5dt01440a.
[42] Pomfret MB, Stoltz C, Varughese B, Walker RA. Structural and compositional characterization of yttria-stabilized zirconia: evidence of surface-stabilized, low-valence metal species. Anal Chem 2005;77:1791–5. https://doi.org/10.1021/ac048600u.
[43] Pagliari M, Marasi M, Donazzi A. Electrocatalytic and operando characterization of state-of-the-art SOFC cathodes for applications at high CO2 concentration in novel clean power production cycles. Electrochim Acta 2024;501:144779. https://doi.org/10.1016/j.electacta.2024.144779.
[44] Opitz AK, Rameshan C, Kubicek M, Rupp GM, Nenning A, Götsch T, et al. The chemical evolution of the La0.6Sr0.4CoO3−Δ surface under SOFC operating conditions and its implications for electrochemical oxygen exchange activity. Top Catal 2018;61:2129–41. https://doi.org/10.1007/s11244-018-1068-1.
[45] Zhang C, Sunarso J, Liu S. Designing CO2-resistant oxygen-selective mixed ionic-electronic conducting membranes: guidelines, recent advances, and forward directions. Chem Soc Rev 2017;46:2941–3005. https://doi.org/10.1039/c6cs00841k.
[46] N. Li, J. Chen, & X. Chen, Y. Lai, C. Yu, L. Yao, Y. Liang, Novel visible-light-driven SrCoO 3 /ag 3 PO 4 heterojunction with enhanced photocatalytic performance for tetracycline degradation, (n.d.). DOI: https://doi.org/10.1007/s11356-021-16338-4/Published.
[47] Irshad MS, Arshad N, Zhang J, Song C, Mushtaq N, Alomar M, et al. Wormlike perovskite oxide coupled with phase-change material for all-weather solar evaporation and thermal storage applications. Adv Energy Sustain Res 2023;4. https://doi.org/10.1002/aesr.202200158.
[48] He M, Alomar M, Alqarni AS, Arshad N, Akbar M, Yousaf M, et al. Strontium-cobaltite-based perovskite (SrCoO3) for solar-driven interfacial evaporation Systems for Clean Water Generation. Nanomaterials 2023;13. https://doi.org/10.3390/nano13081420.
[49] Zhang Z, Sun H, Li J, Shi Z, Fan M, Bian H, et al. S-doped CoMn2O4 with more high valence metallic cations and oxygen defects for zinc-air batteries. J Power Sources 2021;491. https://doi.org/10.1016/j.jpowsour.2021.229584.
[50] Wang C, Zeng L, Guo W, Gong C, Yang J. Enhancing oxygen and hydrogen evolution activities of perovskite oxide LaCoO3: via effective doping of platinum. RSC Adv 2019;9:35646–54. https://doi.org/10.1039/c9ra05491j.
[51] Jiang SP. Development of lanthanum strontium cobalt ferrite perovskite electrodes of solid oxide fuel cells – a review. Int J Hydrog Energy 2019;44:7448–93. https://doi.org/10.1016/j.ijhydene.2019.01.212.
[52] Li P, Huang Q, Yang W, Tian C, Liu Y, Zhao W, et al. The role of the a-site cation on the bifunctional electrocatalytic activities of Ln0.5Sr0.5CoO3-δ (Ln = La, Pr and Sm) for rechargeable zinc–air batteries. Catalysts 2023;13. https://doi.org/10.3390/catal13030483.
[53] Ishii A, Nemoto N, Yamaguchi M, Kobayashi K, Oikawa I, Takano A, et al. Key role of interfacial cobalt segregation in stable low-resistance composite oxygen-reducing electrodes. ACS Appl Mater Interfaces 2023;15:34809–17. https://doi.org/10.1021/acsami.3c04940.
[54] Wang X, Pan Z, Chu X, Huang K, Cong Y, Cao R, et al. Atomic-scale insights into surface lattice oxygen activation at the spinel/perovskite interface of Co3O4/La0.3Sr0.7CoO3. Angew Chem Int Ed 2019;58:11720–5. https://doi.org/10.1002/anie.201905543.
[55] Chen X, Su Q, Yu J, Wei M, Guo G, Wang Y. Experimental study on the degradation mechanism of LaCoO3-based symmetric supercapacitors. RSC Adv 2021;11:25170–8. https://doi.org/10.1039/d1ra03362j.
[56] Błaszczak P, Ducka A, Wolanin B, Matlak K, Machowski G, Prześniak-Welenc M, et al. Fabrication of wormhole-like YSZ and Ni-YSZ by the novel soft-hard template CTAB/NaCl-assisted route. Suppressing Ni coalescence in SOFC. J Eur Ceram Soc 2023;43:438–51.

[57] Faes A, Jeangros Q, Wagner JB, Hansen TW, Van Herle J, Brisse A, et al. In situ reduction and oxidation of nickel from solid oxide fuel cells in a transmission Electron microscope. ECS Trans 2009;25:1985–92. https://doi.org/10.1149/1.3205743.
[58] Chen K, Jiang SP. Surface segregation in solid oxide cell oxygen electrodes: phenomena, mitigation strategies and electrochemical properties. Electrochem Energy Rev 2020;3:730–65. https://doi.org/10.1007/s41918-020-00078-z.
[59] Chou J-T, Inoue Y, Kawabata T, Matsuda J, Taniguchi S, Sasaki K. Mechanism of SrZrO 3 formation at GDC/YSZ Interface of SOFC cathode. J Electrochem Soc 2018;165:F959–65. https://doi.org/10.1149/2.0551811jes.
[60] Siebenhofer M, Riedl C, Nenning A, Artner W, Rameshan C, Opitz AK, et al. Improving and degrading the oxygen exchange kinetics of La0.6Sr0.4CoO3−δ by Sr decoration. J Mater Chem A 2023;11:12827–36. https://doi.org/10.1039/d2ta09362f.